14th International Symposium on Particle Image Velocimetry – ISPIV 2021
August 1–5, 2021

Error propagation dynamics of velocimetry-based pressure field calculations (2): on the error profile

Matthew Faiella[1], Corwin Grant Jeon Macmillan[1], Jared P. Whitehead[2*] and Zhao Pan[1†]

[1] University of Waterloo, Department of Mechanical and Mechatronics Engineering, ON N2L 3G1, Canada

[2] Brigham Young University, Mathematics Department, Provo, UT 84602, USA

[*] whitehead@mathematics.byu.edu [†] zhao.pan@uwaterloo.ca

Abstract

This work investigates the propagation of error in a Velocimetry-based Pressure field reconstruction (V-Pressure) problem to determine and explain the effects of error profile of the data on the error propagation. The results discussed are an extension to those found in Pan et al. (2016). We first show how to determine the upper bound of the error in the pressure field, and that this worst scenario for error in the data field is unique and depends on the characteristics of the domain. We then show that the error propagation for a V-Pressure problem is analogous to elastic deformation in, for example, a Euler-Bernoulli beam or Kirchhoff-Love plate for one- and two-dimensional problems, respectively. Finally, we discuss the difference in error propagation near Dirichlet and Neumann boundary conditions, and explain the behavior using Green's function and the solid mechanics analogy. The methods discussed in this paper will benefit the community in two ways: i) to give experimentalists intuitive and quantitative insights to design tests that minimize error propagation for a V-pressure problem, and ii) to create tests with significant error propagation for the benchmarking of V-Pressure solvers or algorithms. This paper is intended as a summary of recent research conducted by the authors, whereas the full work has been recently published (Faiella et al., 2021).

1 Introduction

Using Particle Image Velocimetry (PIV) to reconstruct the pressure field in a fluid flow has many promising applications (for example, see Zhang and Porfiri (2019); Zhang et al. (2020); Deem et al. (2020); Pereira et al. (2020)). While uncertainty quantification for velocity fields obtained from PIV experiments has been studied in depth (Wieneke, 2017; Raffel et al., 2018; Sciacchitano, 2019), less research has been conducted into assessing uncertainty in the calculated pressure field.

de Kat and Van Oudheusden (2012) provides the first analysis on the error associated with sampling frequency (spatial and temporal) in the context of V-Pressure problems. It was commented that the central finite difference based pressure Poisson solver acts as a low-pass filter, effectively eliminating the high-frequency errors (and signals) in the pressure calculation. The ratio of the grid spacing of the numerical method to the temporal or spatial wave length of the experimental data impacts the frequency response of the pressure Poisson solver. Specifically, high frequency data (or noise) is filtered resulting in the loss of high-frequency physics (or low-pass filtering effect). Similarly, low frequency errors (and signals) are more likely to propagate through the pressure calculation. However, the results are constrained to a 'local' analysis of a specific numerical scheme. The effect of the 'global' setup of the flow domain, including size, shape of the domain and configuration of boundary conditions on the frequency response was not covered.

Pan et al. (2016) analytically discussed how the error in the data field propagates to the calculated pressure field. The upper bounds of the error in the calculated pressure field are derived for different setups. It showed that the error propagation dynamics of a V-Pressure problem can be significantly affected by the 'global' setup of the domain, especially the configuration of the boundary conditions. Under the general analytical framework, this work indicated that the error propagation is also influenced by the error profile in the data field. However, this paper did not identify a worst case error profile in the data field that leads to

the maximum overall error in the calculated pressure field. Moreover, how the error in the data field with different profiles affects the error propagation was not discussed.

In the present work, we show a systematic method for finding the worst case error profile in the data field which causes the most error in the pressure field to be reached. The procedure for finding this worst case (or most dangerous) error in the data field demonstrates how the profile of the error in the data (e.g., spatial frequency and location of error peaks in the domain) combined with the fundamental configuration of the domain (i.e. size, dimension, shape, and boundary condition configuration of the domain) affects the error propagation.

2 Worst case error and the effect of fundamental domain configuration

The error propagation from the data field (ε_f) to the calculated pressure field (ε_p) for a V-pressure problem can be modelled via a Poisson's equation with respect to error (Pan et al., 2016):

$$\varepsilon_f = \nabla^2 \varepsilon_p. \tag{1}$$

The power of the error, averaged over the space of the domain, can be measured by the L^2 norm; for example, the error level of the calculated pressure field is

$$||\varepsilon_p||_{L^2(\Omega)} = \sqrt{\frac{\int \varepsilon_p^2 d\Omega}{|\Omega|}}, \tag{2}$$

where Ω is the domain of the flow field, and $|\Omega|$ is the length, area or volume of the domain, for a 1D, 2D, or 3D problem, respectively. To quantitatively assess error propagation from the data field to the pressure field, the ratio between the error levels pressure field (can be considered as an output) and data field (considered as an input) can be used. Thus, to find the worst case error for a given domain, we seek the function ε_f to satisfy:

$$Ar^* = \max_{\varepsilon_f} Ar = \max_{\varepsilon_f} \frac{||\varepsilon_p||_{L^2(\Omega)}}{||\varepsilon_f||_{L^2(\Omega)}}, \tag{3}$$

subject to (1) with the appropriate BCs on the domain. Ar is the ratio of the error level in the calculated pressure field to the error level in the data (i.e. $Ar = \frac{||\varepsilon_p||_{L^2(\Omega)}}{||\varepsilon_f||_{L^2(\Omega)}}$). We will refer to Ar as the error amplification ratio, and refer to the ε_f function which satisfies (3) as the *worst error*, denoted ε_f^*. The worst error ε_f^* can be thought of as the most dangerous error in the data field that corrupts the pressure field reconstruction most. We will only be considering cases where ε_f is non-zero in order to avoid division by zero, and to reflect the reality that all experimental data will have some error.

As an example, we will consider the optimization problem shown in (3) with pure Dirichlet boundary conditions (note that Neumann or mixed boundaries can be treated similarly). Applying the calculus of variations (Gelfand and Fomin, 1991), we can find that the calculated pressure field will satisfy the Euler-Lagrange equations:

$$\nabla^4 \varepsilon_p = -\frac{1}{\lambda} \varepsilon_p, \tag{4}$$

with $\varepsilon_p = 0$ and $\nabla^2 \varepsilon_p = 0$ on $\partial\Omega$, subject to $|\Omega| ||\nabla^2 \varepsilon_p||^2_{L^2(\Omega)} = 1$, when accurate Dirichlet boundary conditions are applied.

Equation (4) also appears as the characteristic equation of vibrations of elastic bodies (Timoshenko et al., 1937), which will be discussed further in §3. As long as the operator remains self-adjoint, as is the case for the example shown, then there will be a countable number of solutions to the system, each solution corresponding to a natural frequency $\beta_n = \sqrt[4]{-\lambda_n^{-1}}$, where $\lambda_n > 0, n = 1, 2, 3...$ are the eigenvalues. To obtain ε_f^*, the smallest of these eigenvalues $-\lambda_1^{-1}$ is used. The corresponding eigenfunction will be the worst error function which yields the highest possible error amplification ratio. Fundamental configurations of the flow domain, such as the size and shape of the domain, the dimension of the domain, and the type and configuration of boundary conditions will affect the eigenvalue (see also Pan et al. (2016)), and consequently the error propagation.

Table 1: Type of boundary conditions (BCs) of the original pressure Poisson equation, the corresponding BCs of the eigenvalue problem of the worst error and the induced natural boundaries. G, g, H, and h are functions on the boundary $\partial\Omega$, and $\hat{n}$ is the unit outward pointing normal on $\partial\Omega$.

Type of BCs	BCs of pressure Poisson equation	Essential BCs of eigenvalue problem	Natural BCs of eigenvalue problem
Dirichlet	$p = G$	$\varepsilon_p = g$	$\nabla^2\varepsilon_p = 0$
Neumann	$\nabla p \cdot \hat{n} = H$	$\nabla\varepsilon_p \cdot \hat{n} = h$	$\nabla\left(\nabla^2\varepsilon_p\right) \cdot \hat{n} = 0$

The fourth order eigenvalue problem resulting from the fourth order variational problem can be complex and require long calculations even for simple 1D cases. While this calculation may be unfamiliar to fluid mechanics researchers, it has been studied extensively in solid mechanics (e.g., Timoshenko et al. (1937)), taking the form of the Euler-Bernoulli beam problem in 1D, and Kirchoff-Love plate problem in 2D. Tables of solutions for standard boundary conditions and simple domains can be found in several solid mechanics textbooks (e.g. Harris and Piersol (2002)), and would be easy to look up for researchers using Table 1.

In a 1D system with two Dirichlet BCs, for example, the solution to the eigenvalue problem (4) is as follows (see Faiella et al. (2021) for a more detailed derivation):

$$\varepsilon_{f_n} = \pm\sqrt{2}\sin\left(\frac{n\pi}{L}x\right), \quad n = 1,2,3,\ldots \tag{5}$$

which will yield corresponding error in the calculated pressure field:

$$\varepsilon_{p_n} = \pm\sqrt{2}\frac{L^2}{n^2\pi^2}\sin\left(\frac{n\pi}{L}x\right), \quad n = 1,2,3,\ldots \tag{6}$$

Substituting (5) and (6) into (3), the error amplification ratio is

$$Ar = \beta_n^{-2} = \frac{L^2}{\pi^2 n^2}, \quad n = 1,2,3,\ldots \tag{7}$$

Noting the presence of the n^2 term in the denominator of (7), the worst error occurs for the first eigenvalue ($n = 1$ and $Ar^* = L^2/\pi^2$). Thus, the error amplification ratio is larger for lower values of n, which corresponds to lower fundamental frequencies in the data error, while $Ar \to 0$ as $n \to \infty$. The Poisson equation acts as a low-pass filter for the data error, allowing lower frequency error to propagate while eliminating the high frequency errors. Also, the L^2 term in the numerator of (7) shows that the error amplification ratio is increased as the length scale of the domain increases. In general, such a trend also holds for other boundary condition configurations. For example, for a 1D system equipped with one Dirichlet BC and one Neumann BC at each end, the error amplification ratio is

$$Ar = \frac{4L^2}{\pi^2(2n-1)^2}, n = 1,2,3,\ldots \tag{8}$$

and also possesses low-pass filter characteristics.

This low-pass filtering behaviour is a fundamental property of the Poisson equation, and thus will be presented regardless of numerical solving scheme chosen. We wish to emphasize that the frequency response shown in this paper is different than the results obtained when 'local' analysis is used. For example, in de Kat and Van Oudheusden (2012), the amplitude response of a signal or error passing through a Poisson solver is given by:

$$T_{PS}(h,\lambda_x) = \frac{|p|}{|f|} = \frac{|\varepsilon_p|}{|\varepsilon_f|} = \frac{1+\cos\left(\pi\frac{2h}{\lambda_x}\right)}{2\ \mathrm{sinc}\left(\frac{2h}{\lambda_x}\right)}, \tag{9}$$

where T_{PS} is the transfer function of the Poisson solver, h is the grid spacing, and λ_x is the spatial wavelength of the input signal (or error) to the numerical Poisson solver. In (9), as $h/\lambda_x \to 0$, $T_{PS}(h,\lambda_x) \to 1$. This implies that if the mesh is sufficiently fine, the error propagating through a Poisson solver is expected to be unfiltered. This expectation holds only when analysing a local region in a domain and is up to the local choice of

numerical scheme and grid spacing. The analysis in the current work (e.g., (7) and (8) for 1D) is a 'global' result that holds for all numerical pressure Poisson solvers, and complements the aforementioned 'local' analysis. Invoking $\lambda_x \sim 1/n$, $Ar(\lambda_x) = C\lambda_x^2$, where C is a constant which is dependant on the fundamental features of the domain.

3 Analogy to bulking elastic bodies

Interestingly, a parallel can be drawn between the deformation of elastic bodies and the propagation of error in V-Pressure experiments. We next use Euler-Bernoulli beam theory, as a 1D example, to demonstrate the intuitive analogy and evaluate the magnitude of the error propagation in V-Pressure. Consider a homogeneous beam of length L which undergoes transverse vibrations. The normalized deflection profile of the beam is governed by the differential equation:

$$\frac{d^4Y}{dx^4} = \frac{d^2Y}{dt^2}, \tag{10}$$

where $Y(x,t)$ is the beam deflection in the direction that is perpendicular to the x coordinate, and t is time. By separation of variables ($Y(x,t) = X(x)T(t)$), where $T(t)$ is a function of t and $X(x)$ is a function of the spatial x coordinate and hence describes the modes of the vibrating beam, the corresponding eigenvalue problem of (10) is:

$$\frac{d^4X}{dx^4} = \gamma X, \tag{11}$$

where γ is the eigenvalue, and $k = \sqrt[4]{\gamma}$ (Timoshenko et al., 1937) is the spatial frequencies of the buckled beam. Different eigenvalues ($\gamma_n = \omega_n^{-2},\ n = 1,2,3,...$) correspond to different natural frequencies (ω_n) of the vibrating beam and the eigenfunctions (X_n) describe the modes of the beam deflections. Larger eigenvalues correspond to beam modes with higher spatial frequencies. We also recall the normalized governing equations of a bending beam:

$$\frac{dX}{dx} = \Theta, \tag{12}$$

$$\frac{d^2X}{dx^2} = -M, \tag{13}$$

$$\frac{d^3X}{dx^3} = -Q, \tag{14}$$

$$\frac{d^4X}{dx^4} = -W, \tag{15}$$

where Θ is the slope, M is the bending moment, Q is the shear force in the beam, and W is the transverse load on the beam, respectively.

One may notice that (11), which is from Euler-Bernoulli beam theory, is the 1D equivalent of (4), which arises in the error propagation problem of pressure-velocimetry calculations. In addition, (13) describes the relationship between the second order derivative of the beam deflection and bending moment; and it takes the form of the Poisson's equation about error propagation, i.e., (1) in one dimension. We now observe the analogy between the Euler-Bernoulli problem and the dynamics of V-Pressure error propagation, from (13) and (1): the buckling of a beam (X) as a result of an applied bending moment (M) is equivalent to the profile of the error in the pressure field (ε_p) as a result of the error in the data (ε_f) for the V-Pressure error propagation problem.

Solving (11) requires four boundary conditions. For example, if both ends of the beam are simply supported (also called hinged in some textbooks, see figure 1(a) for illustration), the displacement at the ends are constrained by the kinematic boundary conditions (also called essential boundary conditions):

$$X(0) = X(L) = 0, \tag{16}$$

and natural boundary conditions indicating that no bending moments are exerted at the ends (see Harris and Piersol (2002) and (13)):

$$X''(0) = X''(L) = 0. \tag{17}$$

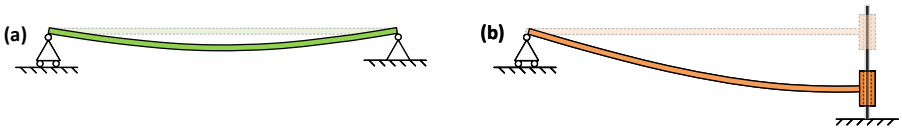

Figure 1: Bent Euler-Bernoulli beam with different supporting mechanisms: (a) simply supported at both ends (associated with Dirichlet-Dirichlet BCs for V-Pressure problem) and (b) simply supported at the left end and supported by a slide at the right end (associated with Dirichlet-Neumann BCs).

We can see that the boundary conditions (16) mimic the essential boundary conditions of the eigenvalue problem (4) that arise from homogeneous boundary conditions, $\varepsilon_p(0) = \varepsilon_p(L) = 0$. Similarly, the boundary conditions (17) mimic the corresponding natural boundary conditions that arise from the calculus of variations $\varepsilon_p''(0) = \varepsilon_p''(L) = 0$. The analogy between beam deflection and V-Pressure error propagation is shown more clearly in Table 2. This table shows the physical interpretation of different variables/equations in the beam problem, as well as their equivalent variables/equations in V-Pressure error propagation. The table also draws the parallel between a homogeneous Neumann boundary in the pressure Poisson equation and a slide-support in elastic dynamics (illustrated in figure 1(b)). The analogy of the buckling of elastic bodies will be further reinforced in the following section (§4) in the context of V-Pressure error propagation.

4 Impact of the location of the error

The dynamics of error propagation to the pressure field from the data field is a function that depends on both the domain's fundamental features and the location of the error. To demonstrate this, we can use a sharp peak error function that is constrained to have a finite error power. For example, the following rectangular peak can be used for 1D analysis:

$$\varepsilon_f = \delta_\Pi(x - x_0) = \begin{cases} \xi, & |x - x_0| \le \frac{\Pi}{2} \\ 0, & |x - x_0| > \frac{\Pi}{2} \end{cases}, \tag{18}$$

where $\delta_\Pi(x - x_0)$ is a rectangular pulse function with a small pulse width Π centered at $x = x_0$. The resulting ε_p and the corresponding error amplification ratio (Ar) for each $x_0 \in (0, L)$ then can be evaluated by solving (1). $Ar = Ar(x_0)$ is thus a quantification of how sensitive the pressure solver is to the error at a given location x_0.

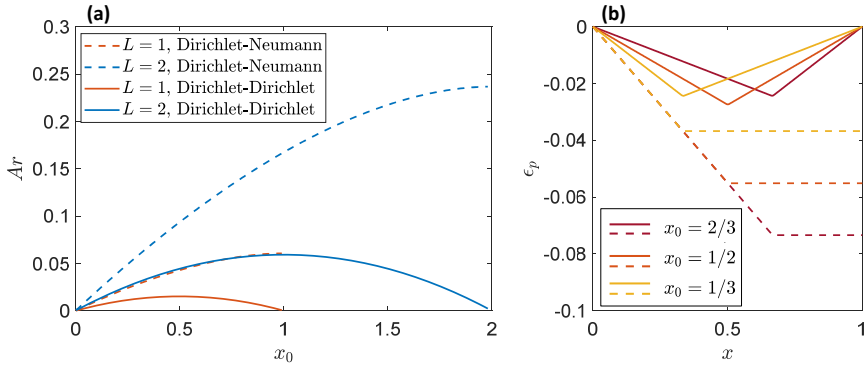

Figure 2: Error amplification ratio (Ar) and error profile in the pressure field ε_p when concentrated error ($\varepsilon_f = \delta_{0.01L}(x - x_0)$ is introduced at different locations (x_0)). (a) Ar corresponding to the location of concentrated error (x_0) for domains with different sizes and configurations of boundary condition. (b) Profiles of ε_p over a domain with size $L = 1$, when concentrated error $\varepsilon_f = \delta_\Pi(x - x_0)$ is introduced at $x_0 = 2/3, 1/2, 1/3$. The solid curves indicate the results on the domain with Dirichlet-Dirichlet BCs, and the dashed curves indicate the results on the domain with Dirichlet-Neumann BCs, respectively.

Figure 2(a) demonstrates a case study of the error amplification ratio $Ar(x_0)$ caused by error concentrated at different places in a 1D domain with different sizes ($L = 1$ or 2) and configurations of boundary conditions.

Table 2: Analogy between the beam vibration problem and the error propagation problem raised by the Velocimetry-based pressure reconstruction.

Physical interpretation	E-B beam vibration problem	Mathematics	V-Pressure error propagation problem	Physical interpretation
Vibration motion of a Euler-Bernoulli beam	$Y'''' = -Y$	Original governing eq.	$\nabla^2 p = f$	Pressure Poisson eq.
Beam deflection due to bending moment	$Y'' = -M$	Induced governing eq. [i]	$\nabla^2 \epsilon_p = \epsilon_f$	Error propagation eq.
Eq. determining modes of the beam	$Y'''' = \gamma X$	4th order eigenvalue problem [ii]	$\nabla^4 \epsilon_p = -\lambda^{-1} \epsilon_p$	Euler-Lagrange eq. determining the worst error in pressure field
Eigenvalues for bending beam	γ_n	Eigenvalues	$-{\lambda_n}^{-1}$	Eigenvalues determined by the Lagrange multipliers
The 1st, 2nd, ... modes of beam deflection	X_n, $n = 1,2,...$	Eigenfunctions	ϵ_{p_n}, $n = 1,2,\cdots$	The worst, 2nd worst... error in the pressure field
The 1st, 2nd, ... modes of bending moment	X_n'', $n = 1,2,...$	2nd order derivative of eigenfunctions	$\nabla^2 \epsilon_{p_n} = \epsilon_{f_n}$, $n = 1,2,\cdots$	The worst, 2nd worst... error in the data field
Hinged end of a beam	$X\ 0\ = 0$	Essential BC [iii]	$\epsilon_p(0) = 0$	Dirichlet BC enforced on a flow domain
	$X'' = 0$	Natural BC	${\epsilon_p}'' = 0$	
Slide-supported end of a beam	$X' = 0$	Essential BC	$\epsilon_p'' = 0$	Neumann BC enforced on a flow domain
	$X''' = 0$	Natural BC	${\epsilon_p}''' = 0$	

[i] The governing equations are normalized to expose the mathematical roots shared by the two problems. For the beam problem, $Y(x,t) = X(x)T(t)$ is the deflection of the beam, which is a function of $x \in [0, L]$, and time $t \in [0, \infty)$. $[\,]'$ indicates the derivative with respect to x, and $[\,]$ indicates the time derivative. For the error propagation problem in V-Pressure, derivation can be found in (Pan et al., 2016).

[ii] The derivations for the Eigenvalue problem can be found in Timoshenko et al. (1937) (for the beam problem) and in Sec. 2 (for the PIV-pressure error problem).

[iii] Homogeneous boundary conditions at $x = 0$ are used as examples.

The concentrated error source is constructed using (18) with width $\Pi = 0.01L$ and height $\xi = 10$. The solid curves, which represent domains with pure Dirichlet boundaries, have the highest value of Ar at the center of the domain, which is the location which is farthest from any Dirichlet boundary, while Ar vanishes as the Dirichlet boundaries are approached. The dashed curves, which represent domains with Dirichlet-Neumann conditions, have the highest value of Ar at the Neumann boundaries, and also have $Ar(x_0)$ approach 0 at the Dirichlet boundaries. This implies that the data near a Dirichlet boundary is less sensitive to error, while data far from Dirichlet boundaries or close to a Neumann boundary is sensitive to error in the data.

Figure 2(b) shows the reconstructed pressure field, ε_p, for a concentrated error located at $x_0 = 1/3, 1/2,$ and $2/3$ for pure Dirichlet (solid lines) and mixed (dashed lines) boundary conditions. The error for the pure Dirichlet case reaches its highest peak for $x_0 = 1/2$, when the concentrated error is furthest from the Dirichlet boundaries. For the mixed boundary conditions, the error reaches its highest value for $x_0 = 2/3$, which is when the concentrated error is closest to the Neumann boundary. The error for the pure Dirichlet case is much lower than the equivalent error for mixed boundary conditions. Figure 2(b) can be thought of in terms of the buckling beam example, where x_0 is the location of an applied moment on the beam, and ε_p is the beam deflection profile. The pure Dirichlet condition would be equivalent to the beam shown in figure 1(a), while the mixed condition would be equivalent to figure 1(b). The beam shown in figure 1(a)

would deflect the most when the moment was applied to its center, just as the error is maximized for the pure Dirichlet condition with error at $x_0 = 1/2$. The beam in figure 1(b) would deflect the most for an error next to the free support, just as the mixed boundary condition has the greatest error for $x_0 = 2/3$. Finally, the beam in figure 1(b) would deflect much more than the beam in figure 1(a) for an equivalent moment, since its free end allows more movement and provides less support than the two "fixed" supports.

This effect of Dirichlet and Neumann boundaries on error propagation is also present in 2 dimensions. The error sensitivity can again be examined using a pulse function of the form:

$$\varepsilon_f = \delta_\Pi(\boldsymbol{x} - \boldsymbol{x_0}) = \begin{cases} \frac{2}{\sqrt{\pi}\Pi}, & |\boldsymbol{x} - \boldsymbol{x_0}| \leq \frac{\Pi}{2} \\ 0, & |\boldsymbol{x} - \boldsymbol{x_0}| > \frac{\Pi}{2} \end{cases}, \tag{19}$$

where $\boldsymbol{x_0} = (x_0, y_0)$ is the coordinate of the center of the concentrated error.

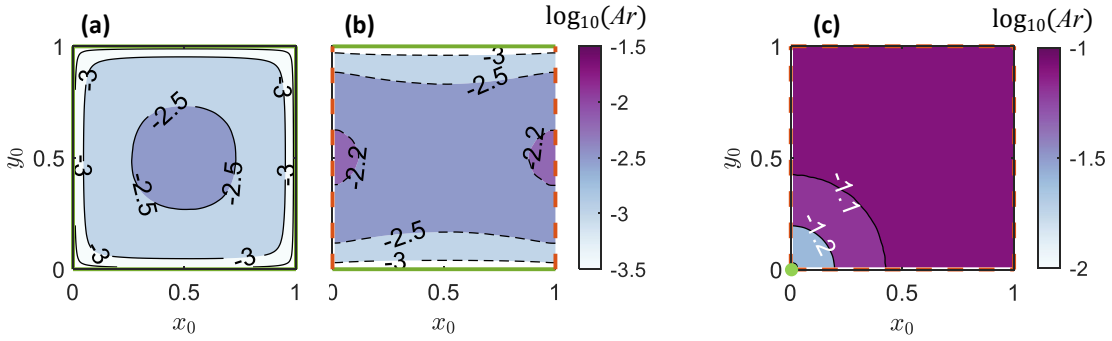

Figure 3: Error amplification ratio $Ar(x_0, y_0)$ responding to concentrated error located at $\boldsymbol{x_0} = (x_0, y_0)$ for domains with (a) pure Dirichlet boundaries and (b) & (c) mixed boundaries, respectively. Dirichlet boundaries are marked by green solid lines in (a) & (b), and the green dot in (c). Neumann boundaries are marked by orange dashed lines.

Figure 3 shows the error sensitivity map on a 1×1 domain for three distinct BC configurations, where $Ar(x_0, y_0)$ is a function of the location of the concentrated error source as illustrated. The concentrated error source is constructed using (19) with a width of $\Pi = 0.02/\sqrt{|\Omega|}$. We again show that error near a Dirichlet boundary is less sensitive in terms of error propagation, while the error near a Neumann boundary and/or far away from a Dirichlet boundary is more dangerous. In figure 3(a), Ar is lowest around the edges of the domain where Dirichlet boundaries are present, while Ar is largest in the center of the domain, far from the Dirichlet boundaries. In figure 3(b), Ar is again low near the Dirichlet boundaries, but increases along the Neumann edges. Ar is highest at the center of the Neumann boundary where proximity to a Neumann boundary is maximized while proximity to a Dirichlet boundary is minimized. Finally, in figure 3(c), Ar is high everywhere in the domain except for the region near $\boldsymbol{x_0} = (0, 0)$, where Ar is tamed by the presence of a Dirichlet boundary.

We now finalize the analogy between the deformation of elastic plates and the V-Pressure error propagation. The behavior of error near boundary conditions can be thought of intuitively using the analogy to a bending beam in 1D or plate in 2D. An accurate Dirichlet boundary on the V-Pressure domain is analogous to a simply supported edge on a plate which constrains the deflection to be vanishing at the boundary. We recall that loads applied next to a simply supported edge cannot deflect the plate much due to the relatively 'firm' support nearby. However, as we move away from this firm support, the plate becomes easier to bend. In contrast, an accurate Neumann boundary on the V-Pressure domain is analogous to a sliding support which allows any amount of deflection but constrains the local slope to be zero. A moment applied near this boundary will deform a large segment of the plate; due to the constraint on the slope of the plate at this boundary, the sliding mechanism will 'pull' on other sections of the plate and bring them along with the loaded section. Long Neumann boundaries are more 'dangerous' than short ones, as this effect is carried out over a longer distance.

These observations about the effect of the distance from an error source to boundaries with different BCs can also be explained using Green's function for the Poisson equation. Consider, in 2D, a concentrated error source in the data field taking the form of the Dirac delta function, $\varepsilon_f = -\delta(\boldsymbol{x_0})$, located at $\boldsymbol{x_0} = (x_0, y_0)$. The error in the pressure field caused by this concentrated error source is the fundamental solution of the

Poisson equation given by the Green's function. When the distance from the error to a nearby boundary is much shorter than the distance to any other other boundaries, the local error near the source (and the nearby boundary) can be approximated by the Green's function on a half plane by the method of images. For example, the Green's function on a half plane with a homogeneous Dirichlet boundary at $x = 0$ is

$$\varepsilon_p = G(\boldsymbol{x}, \boldsymbol{x_0}) = \frac{1}{2\pi} \ln \left[\frac{\langle (x,y), (x_0,y_0) \rangle}{\langle (x,y), (-x_0,y_0) \rangle} \right], \tag{20}$$

where $\langle (x,y), (x_0,y_0) \rangle = \sqrt{(x-x_0)^2 + (y-y_0)^2}$ is the distance from $\boldsymbol{x}$ to $\boldsymbol{x_0}$ (Tikhonov and Samarskii, 2013). As the location of the error approaches the boundary ($x_0 \to 0$), $G(\boldsymbol{x}, \boldsymbol{x_0}) \to 0$ and thus, ε_p vanishes quickly towards the Dirichlet boundary.

For an error source close to a Neumann boundary, the corresponding Green's function on the half-plane is

$$\varepsilon_p = G(\boldsymbol{x}, \boldsymbol{x_0}) = \frac{1}{2\pi} \ln \left[\langle (x,y), (x_0,y_0) \rangle \langle (x,y), (-x_0,y_0) \rangle \right]. \tag{21}$$

As the location of the concentrated error source approaches the Neumann boundary ($x_0 \to 0$), $G(\boldsymbol{x}, \boldsymbol{x_0}) \to \infty$ and ε_p blows up at the Neumann boundary. This irregular behavior is unique to the Green's function analysis and is not physical, as ε_f cannot be a strictly Dirac delta function in reality. Despite this singularity, the mathematical intuition that arises from this analysis shows how the location of the error in the data coupled with the BCs configuration affects the error propagation.

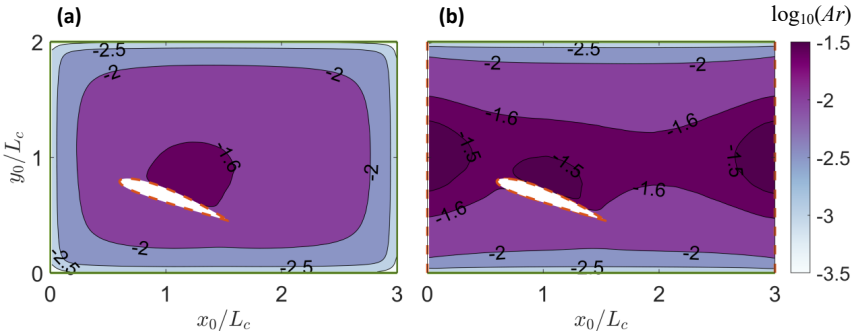

Figure 4: Error amplification ratio $Ar(\boldsymbol{x_0})$ corresponding to concentrated error located at $\boldsymbol{x_0} = (x_0, y_0)$ for domains featuring an airfoil of chord length L_c. Neumann BCs are applied on the surface of the airfoil. The domains feature (a) Dirichlet BCs on the outer boundaries and (b) mixed BCs on the outer boundaries. Dirichlet boundaries are marked by green solid lines and Neumann boundaries are marked by orange dashed lines, respectively.

We further demonstrate the dependence of $Ar(\boldsymbol{x_0})$ to the placement of error ($\boldsymbol{x_0}$) using a more complex domain. Figure 4 shows error sensitivity maps for a 3×2 domain with an airfoil, nondimensionalized by the airfoil chord length, for different BC configurations. $Ar(x_0, y_0)$ is the error amplification ratio as a function of the location of concentrated error as illustrated. Figure 4(a) shows that concentrated error near a Dirichlet BC is tamed by the boundary, as seen by the low value of amplification ratio Ar around the edges of the domain. Concentrated errors far from Dirichlet boundaries and/or close to a Neumann boundary show more propagation, and thus a higher value of Ar occurs near the center of its domain. In figure 4(b), we see that error amplification is highest in the middle of 'long' Neumann boundaries such as the left and right edges of the domain as well as the suction and pressure surface of the airfoil. The leading edge of the airfoil can be considered a 'short' Neumann boundary due to its high curvature, and thus shows less propagation than these long Neumann boundaries.

Figure 5 shows the reconstructed pressure field for a concentrated error located at different coordinates. In figure 5(a)-(c), the outer boundaries are Dirichlet, while the airfoil boundaries are Neumann. Figure 5(a) shows the effect of concentrated error near a Dirichlet boundary; error rapidly dissipates as the Dirichlet boundary is approached, and does not significantly propagate and contaminate the whole pressure field. In contrast, figure 5(b) shows a concentrated error near a long Neumann boundary, where the error is amplified due to its proximity to a Neumann boundary and the center of the domain and contaminates a large area of the domain. Figure 5(c) also shows a concentrated error near a Neumann boundary, however the pressure

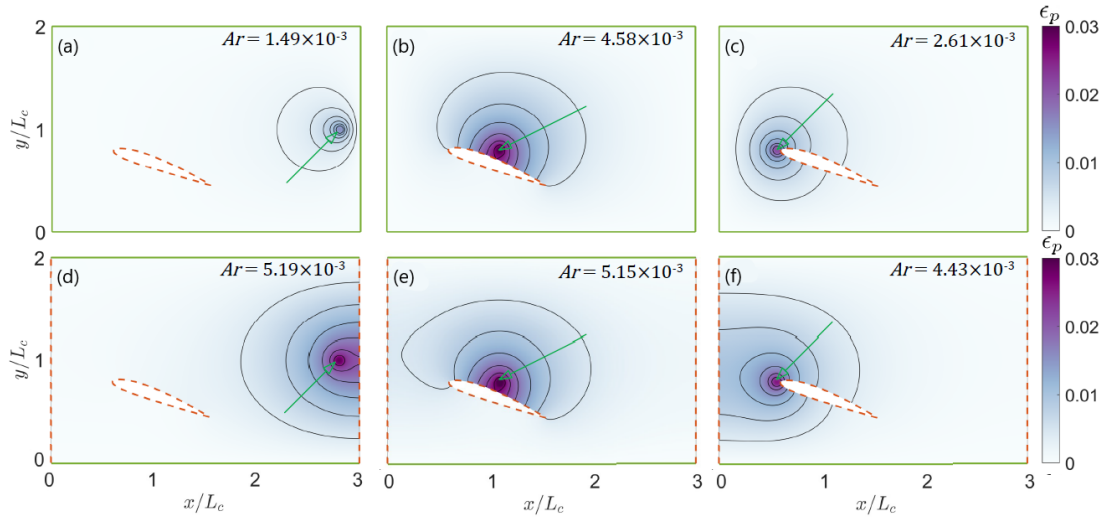

Figure 5: Error in the reconstructed pressure field (ε_p) caused by concentrated error in the data field located at different locations ($\varepsilon_f = \delta(x_0, y_0)$). The type of BCs of the domain are indicated by green solid lines for Dirichlet boundaries, and dashed orange lines for Neumann boundaries. The locations of the error (x_0, y_0) are marked by the green arrow heads. The legend in each subplot indicates the error amplification ratio ($Ar = ||\varepsilon_p||_{L^2(\Omega)}/||\varepsilon_f||L^2(\Omega)$) corresponding to the the ε_f at each location.

field is less contaminated than figure 5(b). This is due to the high curvature of the boundary at this point, which is considered a "short" Neumann boundary and thus the error spreads less. In figure 5(d)-(f), the outer boundaries are mixed boundary conditions, while the airfoil remains as a Neumann boundary. The error shown in figure 5(d) is now beside a Neumann boundary instead of the Dirichlet boundary in figure 5(a). As a result, the error propagates much more and the Ar is greater. In figures 5(e) and (f), we see that the concentrated error propagates more than the error in figure 5(b) and (c). This is because the taming Dirichlet boundaries are lost and replaced with amplifying Neumann boundaries, so error propagates much more freely.

5 Conclusion

In the current work, we present a systematic method for finding the worst case error profile in the data field which causes the most error in the pressure field. This is corresponding to the upper bound of the error in the calculated pressure field discussed in Pan et al. (2016). The worst case error profile in the data field can be found by solving an eigenvalue problem derived from an Euler-Lagrange equation maximizing the the error propagation. The procedure for finding the worst error in the data field shows how the profile of the error in the data (e.g., spatial frequency and location of error peaks in the domain) coupling with the fundamental features of the domain (i.e. size, dimension, type of BCs) affects the error propagation. We show that the Euler-Lagrange equations used to find the worst error function lead to the same eigenvalue problem from the buckling of an Euler-Bernoulli beam in 1D and a Kirchoff-Love plate in 2D. The data field error can be thought of as a bending moment applied to an elastic body, with the resulting pressure field being equivalent to the deformation of the elastic body. Thus, being familiar with the theories of elastic beams and plates (Timoshenko et al., 1937) can be useful in understanding error propagation in V-Pressure problems in a more intuitive way.

We point out that error propagation is significantly affected by the location of the error and the error proximity to Dirichlet and/or Neumann boundaries. This behavior can be explained by finding Green's function for the Poisson equation using the method of images. This result can also be explained intuitively using the solid mechanics analogy. All results in this work represent fundamental properties of the Poisson equation, which hold regardless of experimental setup and choice of numerical solver. The results and analogy-based method can help experimentalists studying fluid mechanics to design better tests which avoid error profiles similar to the worst case, and limit the error in sensitive locations, thus improving overall

accuracy and robustness of the test. In addition, the results can be used to create worst case scenarios and challenging test cases to benchmark V-Pressure solvers or algorithms.

Finally, we emphasize that the present work studies how error in the data field propagates to the reconstructed pressure field. How to interpret error in the data field (ε_f) from the error in the velocity field ($\varepsilon_{\boldsymbol{u}}$) can be challenging. The error propagation analysis from velocity to data ($\varepsilon_{\boldsymbol{u}} \rightarrow \varepsilon_f$) involves the temporal and spatial resolution of velocimetry and specific numerical schemes that evaluate gradients, and thus is out of the scope of the current analytical research. We will leave this topic for future studies, however, some relevant results can be found in, for example, McClure and Yarusevych (2019) and Pan et al. (2018).

References

de Kat R and Van Oudheusden B (2012) Instantaneous planar pressure determination from PIV in turbulent flow. *Experiments in fluids* 52:1089–1106

Deem EA, Cattafesta III LN, Hemati MS, Zhang H, Rowley C, and Mittal R (2020) Adaptive separation control of a laminar boundary layer using online dynamic mode decomposition. *Journal of Fluid Mechanics* 903:A21

Faiella M, Macmillan CGJ, Whitehead JP, and Pan Z (2021) Error propagation dynamics of velocimetry-based pressure field calculations (2): on the error profile. *Measurement Science and Technology* 32:084005

Gelfand IM and Fomin SV (1991) *Calculus of Variations*. Dover

Harris CM and Piersol AG (2002) *Harris' shock and vibration handbook*. volume 5. McGraw-Hill New York

McClure J and Yarusevych S (2019) Generalized framework for piv-based pressure gradient error field determination and correction. *Measurement Science and Technology* 30:084005

Pan Z, Whitehead J, Thomson S, and Truscott T (2016) Error propagation dynamics of piv-based pressure field calculations: How well does the pressure poisson solver perform inherently?. *Measurement Science and Technology* 27:084012

Pan Z, Whitehead JP, Richards G, Truscott TT, and Smith BL (2018) Error propagation dynamics of piv-based pressure field calculation (3): What is the minimum resolvable pressure in a reconstructed field?. *arXiv preprint arXiv:180703958*

Pereira LTL, Ragni D, Avallone F, and Scarano F (2020) Pressure fluctuations from large-scale PIV over a serrated trailing edge. *Experiments in Fluids* 61:1–17

Raffel M, Willert CE, Scarano F, Kähler CJ, Wereley ST, and Kompenhans J (2018) *Particle image velocimetry: a practical guide*. Springer

Sciacchitano A (2019) Uncertainty quantification in particle image velocimetry. *Measurement Science and Technology* 30:092001

Tikhonov AN and Samarskii AA (2013) *Equations of mathematical physics*. Courier Corporation

Timoshenko S et al. (1937) Vibration problems in engineering. Technical report

Wieneke B (2017) *PIV uncertainty quantification and beyond*. Ph.D. thesis. Delft University of Technology

Zhang J, Brindise MC, Rothenberger S, Schnell S, Markl M, Saloner D, Rayz VL, and Vlachos PP (2020) 4d flow mri pressure estimation using velocity measurement-error-based weighted least-squares. *IEEE Transactions on Medical Imaging* 39:1668–1680

Zhang P and Porfiri M (2019) A combined digital image correlation/particle image velocimetry study of water-backed impact. *Composite Structures* 224:111010